 doi:10.20944/preprints202211.0040.v1

Article

Towards Outdoor Electromagnetic Field Exposure Mapping Generation Using Conditional GANs

Mohammed Mallik[1*], Angesom Ataklity Tesfay[2], Benjamin Allaert[2], Esteban Egea-Lopez[3], Jose-Maria Molina-Garcia-Pardo[3], Redha Kassi[1], Joe Wiart[4], Davy P. Gaillot[1], and Laurent Clavier[1,2]

[1] Univ. Lille, CNRS, UMR 8520 - IEMN, Lille, France (e-mail: firstname.name@univ-lille.fr)
[2] IMT Nord Europe, Lille, France (e-mail: firstname.name@imt-nord-europe.fr)
[3] Universidad Politécnica de Cartagena (UPCT), Spain (e-mail: firstname.name@upct.es)
[4] Chaire C2M, LTCI, Télécom Paris, Institut Polytechnique de Paris, Palaiseau, France (email: firstname.name@telecom-paris.fr)
* Correspondence: Mohammed Mallik (email: firstname.name@univ-lille.fr)

Abstract: With the ongoing fifth-generation cellular network (5G) deployment, electromagnetic field exposure has become a critical concern. However, measurements are scarce, and accurate electromagnetic field reconstruction in a geographic region remains challenging. This work proposes a conditional Generative Adversarial Network to address this issue. The main objective is to reconstruct the electromagnetic field exposure map accurately according to the environment's topology from a few sensors located in an outdoor urban environment. The model is trained to learn and estimate the propagation characteristics of the electromagnetic field according to the topology of a given environment. In addition, the conditional Generative Adversarial Network based electromagnetic field mapping is compared with simple kriging. Results show that the proposed method produces accurate estimates and is a promising solution for exposure map reconstruction.

Keywords: EMF exposure; conditional generative adversarial network; optimization

1. Introduction

Wireless communication systems have become an inherent part of our daily life. Hence, monitoring the status of wireless systems phenomena, such as radio-frequency electromagnetic field (RF-EMF) exposure, is of great significance. In urban environments, there are many sources of EMF, including WiFi, 2G, 3G, 4G, and 5G mobile communication technologies. If 5G promises many improvements compared to previous generations [1–3], there is growing anxiety regarding implementing the 5G network for two main reasons. The first one is that the frequency used is higher than the other mobile communication generations. The second reason is the ultra-dense base station implementation requirement. Several organizations, such as the International Commission on Non-Ionizing Radiation Protection (ICNIRP) and the Institute of Electrical and Electronics Engineers (IEEE), have conducted research on human exposure standards for EMFs, as mobile devices and base stations emitting EMFs for radio communication must comply with regulatory human exposure levels for EMFs [4,5].

Although sensor networks and on-site measurements are essential, they are confined systems that only allow a limited amount of EMF exposure monitoring. Locations of base stations and mobile devices in an urban setting are influenced by elements including building topology, roadways, vehicles, and urban city topology. To evaluate RF-EMF exposure, a power map must be constructed while taking these relevant factors into account. The challenge is reconstructing the EMF exposure map in an urban area from only a few sparsely located sensor-measured power values changing over time according to environment topology and network activity.

In this work, we aim to assess the RF-EMF exposure using only 50 fixed receivers sparsely located in a 1 km square urban environment, specifically in Lille city center, France.

 doi:10.20944/preprints202211.0040.v1

This is achieved using a conditional Generative Adversarial Network (cGAN) [6] architecture where the city topology is used as a conditional input. The proposed Exposure Map Generative Adversarial Network (EMGAN) method is an innovative approach inspired by the cGAN architecture. The EMGAN model learns and then estimates the features of outdoor wireless propagation, including diffraction, shadowing reflection, and the impact of building walls, materials, roadways, and city topography.

In this work, we consider a specific frequency band (around 5.89 GHz), this approach can naturally be extended to study the EMF exposure of other technologies (or the combinations of several). Additionally, other reconstruction techniques, such as kriging, are developed to evaluate and compare the with the proposed model.

The main contributions of this paper can be summarized as follows:

- Generating a new simulated dataset, called "LilleExposureMap", which consists of EMF exposure maps in Lille, France.
- Develop the generator and discriminator for the proposed EMGAN utilizing the deep convolutional structure and auto-encoders analogy to learn about signal propagation and calculate the map of EMF exposure.

The performance of the designed EMGAN is evaluated and shows a good reconstruction despite a reduced number of fixed sensors. The paper is organized as follows. In Section 2, the review of related works is discussed. In Section 3, the data set is described. Section 4 describes the proposed EMGAN model. The results and findings are presented and discussed in Section 5. Section 6 concludes the work.

2. Related work

Accurate radio frequency power map estimation is computationally expensive in a geographic region. Predicting power coverage in urban areas typically requires ray-tracing and also empirical/semi-empirical models, such as close-in(CI), floating intercept (FI), alpha, beta, gamma (ABG)[7–9], etc. simulations to determine how radio signals propagate and are distributed over an area. Deterministic and empirical models are used for propagation prediction in earlier studies. Some examples are dominant path model [10], ray-tracing [11,12], and empirical models, such as [13]. Ray-tracing (RT) techniques offer the highest degree of precision, but often at the expense of high processing demands and a reliance on the accuracy of the tridimensional (3D) model of the [14]. RT techniques describe the propagating field as a series of propagating rays that reflect, diffract, and scatter over various environmental components. This high-frequency approximation (optical ray) to the Maxwell equations is the foundation for these approaches. This methodology has often proven computationally too expensive to be employed in large and, in particular, dynamic contexts, hence network simulators only provide stochastic or streamlined hybrid approaches [15]. If they are well suited to the coverage maps, they can not be used for exposure maps, which would require the simulation of many different technologies and the consideration of the number and positions of active users.

Data-driven interpolation methods presume that some measurements are given at specific locations. These methods predict the function at non-measured locations via some signal processing approach, e.g., Kriging [16] relies on a model of the physical characteristics. The work in [17] used kriging to perform spatial interpolation of climate data. The method works well when significant measurement points are considered. In [18], kriging is applied to spatially reconstruct the EMF in an indoor scenario. However, the authors concluded that the reconstruction performance of the model could be improved by increasing the measurement points.

In [19], the authors use a CNN-based Generative Adversarial Network (GAN) [20] to estimate the power spectrum map while considering urban cognitive radio networks. The employed bandwidths are 25 MHz and 75 MHz, and a uniform distribution of users was assumed. The under-sampled power spectrum maps were used as input for the image reconstruction task using a GAN model based on an autoencoder analogy. However, the authors used the inverse polynomial law model in calculating power spectrum maps

Preprints (www.preprints.org) | NOT PEER-REVIEWED | Posted: 2 November 2022 doi:10.20944/preprints202211.0040.v1

(PSMs) to depict propagation characteristics. Additionally, the authors did not consider the topology as conditional input.

For estimating radio maps, two recent papers proposed deep learning approaches [21,22]. The authors implemented a convolutional neural network [23] as the mapping function to estimate the radio map for each Tx-Rx location. Every trained network defines a specific map, and a new city map is needed to train the network. Other works on power map prediction use fully connected neural networks, which do not consider the city topology as additional information [24–26]. In addition, the authors in [27] used a convolutional autoencoder [28] network for spectrum map interpolation, where several transmitters with unknown locations operate. Buildings were superimposed on the estimated map after the model inference. So far in the literature, all the works did not consider the propagation characteristics of the area of interest, which can help to make the accurate mapping. However, in the proposed method, the city topology is considered a conditional input to the cGAN model to represent the urban environment characteristics. To the best of our knowledge, no study in the literature considers the environment topology as additional input.

3. Dataset and Simulator

This work presents a new dataset, called "LilleExposureMap" of 6006 simulated EMF exposure maps in Lille, France, obtained from Veneris-Opal. Different moving transmitter positions are used in order to generate different maps. The considered number of simulated EMF exposure maps is fixed to minimize the computational complexity. One km square area is selected where three different simulations are done, placing three different moving positions of transmitters in the area of interest (see Figure. 1).

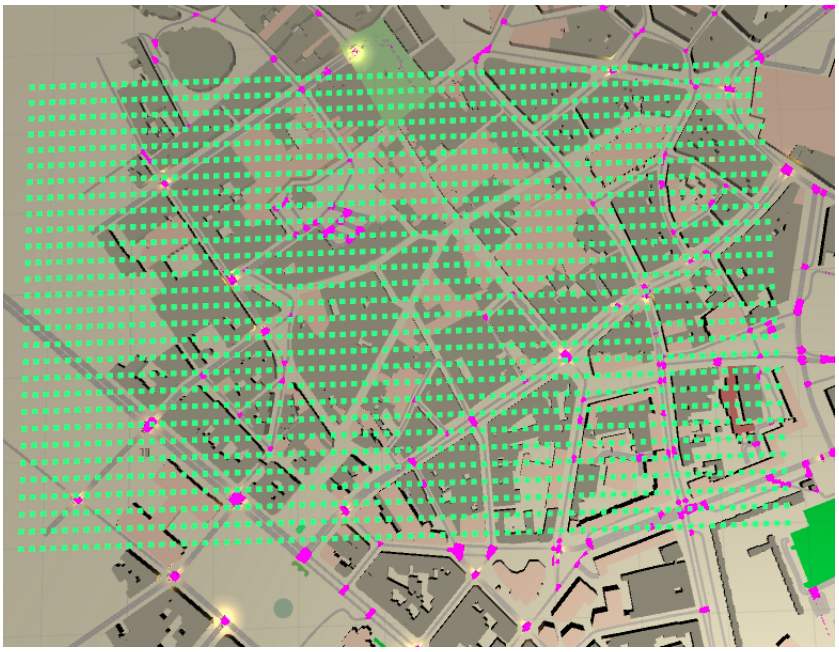

Figure 1. 3D environment model of Lille City 1 km^2 area with 2088 receiver grid represented in green squares.

The 3D environment model is implemented in ' VENERIS -OPAL' an open-source ray tracing network simulator [29]. Veneris-Opal is a simulation framework for research on Vehicular Networks and Cooperative Automated Driving. However, it can also be used for general wireless network simulation, which needs 3D environment-aware propagation simulation. On top of the Unity game engine citehaas2014history, it includes a realistic vehicular model and a set of driving and lane change behaviors that reproduce the traffic dynamics integrated using SUMO [30], a ray-launching GPU-based propagation simulator

Preprints (www.preprints.org) | NOT PEER-REVIEWED | Posted: 2 November 2022 doi:10.20944/preprints202211.0040.v1

called Opal [31] and a set of modules that enable bidirectional coupling with the widely used OMNET++ network simulator.

A map of Lille city center from OpenStreetMap [32] is used for the ray launching simulations in Veneris-Opal. More specifically, the dataset contains objects with rough surfaces like 3D building walls, statues, roads, etc., interacting with the rays in complex ways. Moreover, gaps in the object, e.g., bridges and rays at different levels, can pass or reflect from such objects. The presence of the object in the environment, and several ray interactions result in a complex power distribution representing a real-life environment. The transmitters are assumed to use an isotropic antenna, producing omnidirectional radio waves. The height and power of the transmitting antenna were set at a maximum of 15 meters and 20 Watts, respectively. The propagation model in ray launching considers reflections on 3D buildings, resulting in more complex patterns. Even if VENERIS can handle a very high number of iterations, a convergence study shows that 2 interactions are enough for reliable results in this kind of environment.

For simulations, three transmitters are used at 5.89 GHz with 20 W transmitting power, and other simulation parameters are used, like azimuth, elevation, reflection, etc. To generate the ground truth maps, 2088 receivers at the height of 1.5 meters are placed in a uniform grid in the area of interest, as shown in Figure 1. The receivers inside the buildings are not considered.

Using Veneris-Opal, the received power in a dense urban environment by ray tracing is simulated and converted into images using Python. Then, it is employed as a reference map. Figure 2 gives an example of reference exposure maps when the transmitter is located at the top right corner. Each map has a dimension of 512 height, 512 width, and 3 RGB color channels.

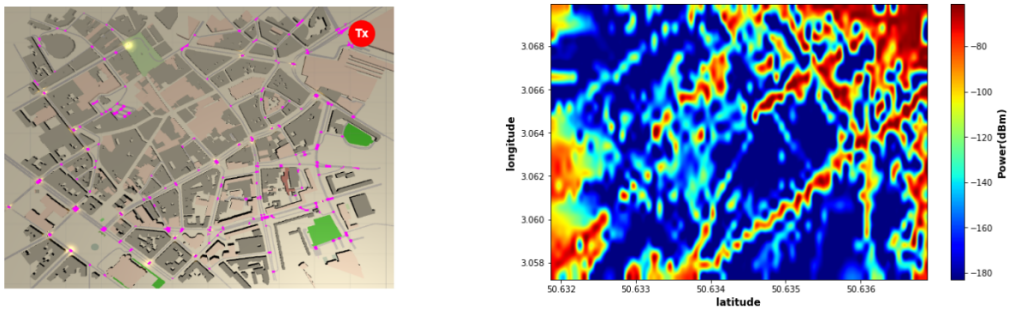

(a) Transmitter's location corner **(b)** Transmitter at upper right corner

Figure 2. RF-EMF exposure reference map.

The area of interest, Lille city center, is 1 km square, and 50 sensor points were selected using 'SensorLocator' an open source web application developed in IRCICA lab by authors which were then extracted from the reference map to generate the undersampled sensor map images. The locations of the sensors are constrained by the position of the lighting poles and are shown in Figure 3, and we consider 15, 30, and 50 fixed locations taken from the reference map images for generating the test set. To capture the city topology effect, we used an image where black and white represent buildings and roads, respectively (with no intermediate grey levels) as a conditional input to the cGAN network. An example of the topology image is shown in Figure 4b, and the EMF map with city topology overlaid is illustrated in Figure 4c. It is important to note that less than 1% of the reference image area in terms of pixels is covered by sensors in the most optimistic case, i.e., when 50 measurements are taken into account.

Preprints (www.preprints.org) | NOT PEER-REVIEWED | Posted: 2 November 2022 doi:10.20944/preprints202211.0040.v1

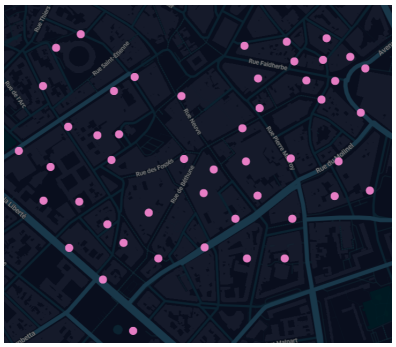

Figure 3. 50 sparsely located sensor map in Lille city center.

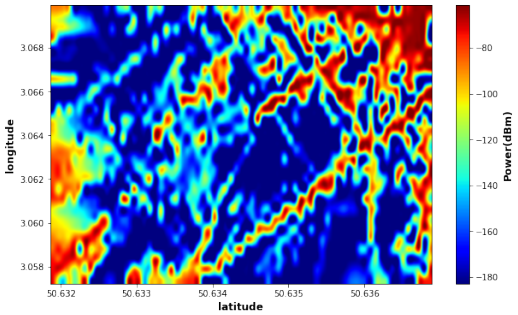

(a) Reference map.

(b) City topology.

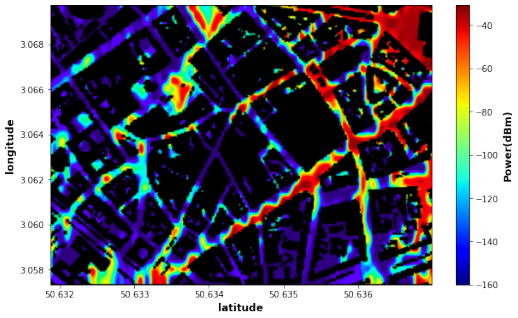

(c) Map superimposed on city topology.

Figure 4. RF-EMF exposure reference map.

4. The Proposed EMGAN Model

We propose a deep learning method inspired by a conditional GAN architecture adapted to image-to-image translation. Several studies have been done using this specific model architecture[33–35] for different applications. In this work, the network learns to estimate the propagation of an electromagnetic field according to a distribution of sensors. Our model is conditioned by a map that represents the topology of a city, thus forcing the model to adapt to a targeted topology, whether indoor or outdoor. Figure 5 illustrates an overview of the proposed method.

4.1. Input and output data

To train the model, input data for the generator are the sensor map and city topology images with a dimension of $512 \times 512 \times 3$. The output is a fake full-exposure map image.

For the discriminator, inputs are the generated fake images from the generator and the real full exposure map image simulated by Veneris-Opal with a dimension of $512 \times 512 \times 3$. The output is classified as whether the data is fake or real, estimated full exposure map.

Preprints (www.preprints.org) | NOT PEER-REVIEWED | Posted: 2 November 2022 doi:10.20944/preprints202211.0040.v1

4.2. Network Architecture

4.2.1. U-Net Generator

Estimating the EMF exposure map is an image-to-image translation task. The model's inputs consist of two images, a sparse sensor measurement map, and the city topology as a conditional input to the generator (the U-net model), represented as a three-dimensional matrix (height, width, and color channel). Three channels—red, green, and blue—are combined to create a picture[36]. A channel represents the color and color intensity of an image. The proposed method reconstructs the final image using a three-dimensional image tensor with three channels. The input sensor measurement map is sparse because each pixel's color intensity corresponds to a sensor-measured value at that location.

Since estimating the EMF exposure map is mainly an image-to-image translation task, the model's inputs are two images, a sparse sensor measurement map, and the city topology as a conditional input to the generator (the U-net model) represented as a three-dimensional matrix, (height, width, and color channel). An image is built by combining three channels, i.e., red, green, and blue [36]. Simply put, a channel refers to color intensity and color in the image. In contrast, a three-dimensional image tensor with channel depth three is utilized for our method to reconstruct the output image. The color intensity of pixels of the input image represents the sensor-measured value at a corresponding location, making the input sparse sensor measurement map. The generator is an encoder-decoder model

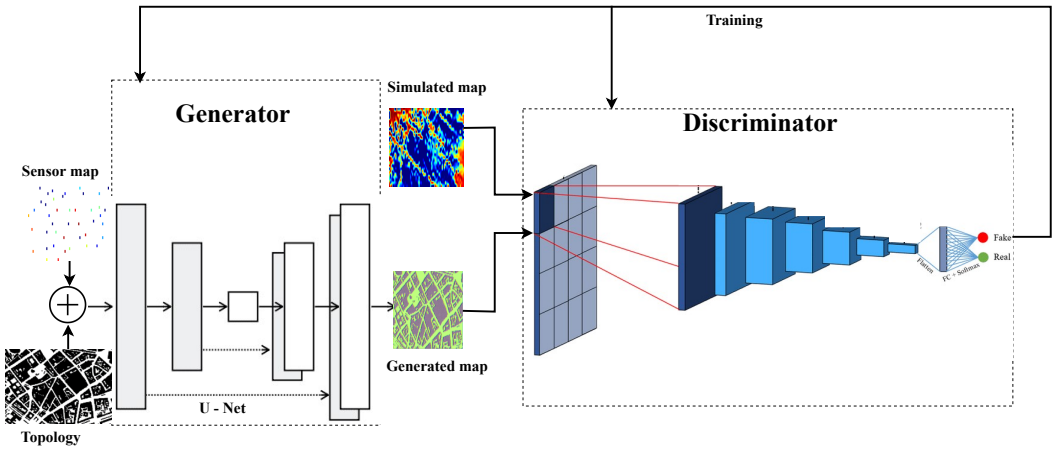

Figure 5. Proposed conditional GAN.

using a U-Net architecture. The model takes a source image (e.g., a sensor map) along with a city topology image as a conditional input and generates a target image (e.g., a complete exposure map with the effect of topology). It does this by first downsampling or encoding the input image down to a bottleneck layer, then upsampling or decoding the bottleneck representation to the size of the output image. Moreover, skip-connections are added between the encoding and corresponding decoding layers for learning features from input images. The model is built to learn more intricate wireless propagation aspects of the target area, and translate it to an EMF map for exposure assessment.

Encoder: The sensor map I s the input to the encoder's input layer. The decoder module consists of several blocks, each of which has following setup:

- Using a kernel size of 3×3 and a stride of 1, two convolutional layers are applied in succession. The input layer uses tensors of a size of $512 \times 512 \times 3$, which represent a three-dimensional sensor map picture. This results in new dimensions with 16 channels and raises the feature map's channel count.
- The rectified linear unit(ReLU) is the activation function that is being used. This function enables to take only positive values after convolution operation.

Preprints (www.preprints.org) | NOT PEER-REVIEWED | Posted: 2 November 2022 doi:10.20944/preprints202211.0040.v1

- A max-pooling layer connects previous layers. This layer downsamples the feature map by taking the biggest value in each patch of each feature map. This creates new dimensions of $64 \times 64 \times 16$.

The first block's layers are repeated in the decoder module, where the depth or channel number rises to $8 \times 8 \times 512$ and the size of the feature map rapidly decreases.

Decoder: Five symmetric reduction module blocks are employed in the decoder module along with a transposed convolutional layer for upsampling. The feature map's height and width are set in the layer's properties to be doubled, but the depth (number of channels) is set to be decreased by half. For the purpose of extracting more precise features from the feature map, two consecutive convolutions are used. The symmetric U-shaped generator model architecture contains five blocks on each module.

4.2.2. Discriminator

The discriminator is a deep convolutional neural network in cGAN explicitly used for conditional image classification. It takes all 3 images as input, the sparse sensor map, the target image, and the conditional topology image. It estimates the likelihood of whether the target image is real or a fake translation of the source image having the effect from the topology as well. The effective receptive field of the model is the core of designing the discriminator. This is called a PatchGAN [35] model, which defines the connection between one output of the model to the number of pixels in the input image. The output estimate of each model corresponds to a 70×70 square or patch of the input image. This method has the advantage that the same model may be used to process input images that are bigger or less than 256×256 pixels. The size of the input image determines whether the discriminator's output is a single value or a square activation map of values. Each value represents the chance that a patch in the input image is real. These values can be averaged if necessary to provide a global probability or categorization score.

4.3. Loss Functions

The loss function of the proposed cGAN model contains the discriminator and the generator part as shown in (1):

$$L_{cGAN}(G, D) = E_{x,y}[\log D(x, y)] + E_{x,z}[1 - \log D(x, G(x, z)] \quad (1)$$

where x is the input image, y is the output image, and z is the conditional image.

The generator G is not only trying to reduce the loss from the discriminator but also trying to move the fake distribution close to the real distribution by using L1 loss which is given in (2):

$$L_{L1}(G) = E_{x,y,z}[\|y - G(x, z)\|] \quad (2)$$

The loss function of generator network is stated in (3):

$$G^{\star} = \arg \min_{G} \max_{D} L_{cGAN}(G, D)\lambda_{L1}(G) \quad (3)$$

5. Results

5.1. Training set-up

For the input training samples, 50 sensor measurement locations are used. Training parameters are listed in Table 1.

5.2. Evaluation metrics

The structural similarity index (SSIM)[37] and peak signal-to-noise ratio (PSNR) are between reconstructed map and the reference map in order to assess the model performance. Values between -1 and 1, where 1 denotes perfect resemblance, are provided by the SSIM model, which captures the observed change in the structural information of the picture.

Preprints (www.preprints.org) | NOT PEER-REVIEWED | Posted: 2 November 2022 doi:10.20944/preprints202211.0040.v1

Table 1. Training parameters.

Parameters	Value
Total number of images	9009
Input samples	2500
Test set	503
Optimizer	ADAM
Learning rate	4×10^{-4}
Batch size	2
Decay rate	1×10^{-6}
Epochs	4000

The PSNR test compares the distortion power to the greatest possible pixel intensity. The SSIM index is calculated on various windows of an image. The measure between two windows x and y of common size $N \times N$ is given below along with PSNR:

$$\text{PSNR} = 10 \log_{10} * \frac{\text{MAX}_\text{I}^2}{\text{MSE}} \tag{4}$$

where MAX_I is the maximum possible pixel value of the image. When the pixels are represented using 8 bits per sample, this is 255. The degree of inaccuracy in statistical models is measured by the mean squared error, or MSE. Between the observed and estimated values, it evaluates the average squared difference. The MSE is equal to 0 when a model is error-free. Its value increases when model error does as well. The mean squared deviation is another name for the mean squared error (MSD).

$$\text{SSIM(x,y)} = \frac{(2\mu_x\mu_y + c_1)(2\sigma_{xy} + c_2)}{(\mu_x^2 + \mu_y^2 + c_1)(\sigma_x^2 + \sigma_y^2 + c_2)} \tag{5}$$

where, μ_x and μ_y are the pixel sample mean of x and y, μ_y. σ_x^2 and σ_y^2 are the variance of x and y, σ_{xy} is the covariance of x and y. $c_1 = (k_1 L)^2$ and $c_2 = (k_2 L)^2$ are the variables to stabilize the division with weak denominator, where L is the dynamic range of the pixel-values. k_1 and k_2 are set to 0.01 and 0.03.

Finally, we will consider the pixel-to-pixel error that we will denote by R. To calculate R, in dB, given by:

$$R(x, y) = 10 \log_{10} \left(\frac{x}{y} \right) \tag{6}$$

We will represent either the probability distribution of R or the cumulative distribution of $|R|$. This allows to have a more detailed understanding of the error behaviour.

5.3. Visual analysis

The proposed EMGAN model is compared with the EME-Net model in [38] and the kriging method when only 50 measurement points are considered. All models are trained and tested on the same training and test data sets. As illustrated in Figure 6, the proposed EMGAN model outperforms the kriging model. The EMGAN-based (6d) reconstructed map looks very close to the ground truth, and few details are missed by the EME-Net-based (6c), whereas the kriging-based (6b) encounters significant loss.

Additionally, the proposed EMGAN model performance is analyzed by varying the number of measurement points. Figure 7 shows the EMGAN-based reconstructed maps using 15 and 30 sensor measurement points. The figure illustrates that the performance of the proposed EMGAN model remains consistent even when a few measurement points are considered, although some degradation can be observed.

The error map between the reconstructed map and the ground truth is illustrated in Figure 8. The error map shows that the proposed EMGAN model (8c, 8d and 8e) has a significantly low error compared to the other models. The kriging approach exhibits very

Preprints (www.preprints.org) | NOT PEER-REVIEWED | Posted: 2 November 2022 doi:10.20944/preprints202211.0040.v1

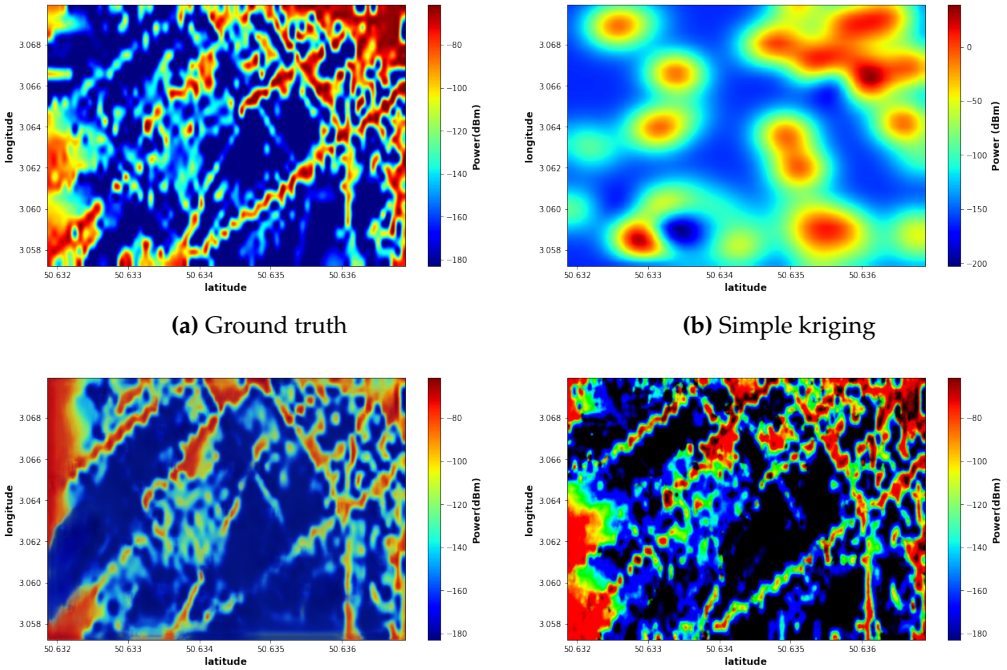

(a) Ground truth **(b)** Simple kriging

(c) EME-Net model **(d)** Proposed EMGAN model

Figure 6. Comparison of Reconstructed maps of the proposed model and other different models.

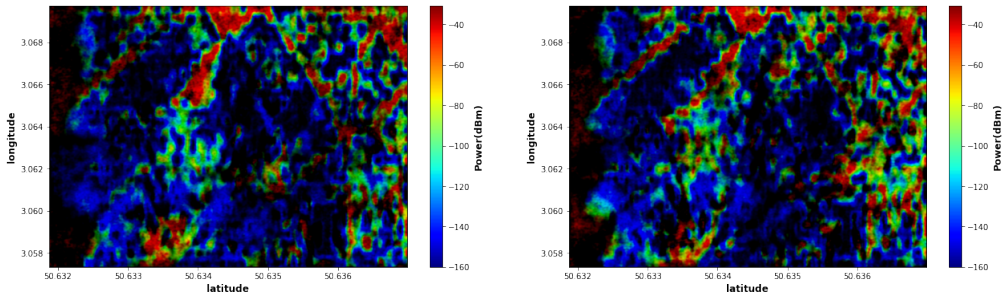

(a) Using 15 sensor map **(b)** Using 30 sensor map

Figure 7. EMGAN-based Reconstructed maps when different number of sensors are considered.

poor results. The approach is not well adapted with such a spatial undersampling. Further studies, though, should be done to take into consideration the environment topology and the propagation models. This however is a different approach and is out of the scope of this paper.

5.4. Quantified Analysis

Figure 9 presents the averages of SSIM and PSNR as a function of the number of measurement points. As the number of measurement points rises, so do the averages of SSIM and PSNR. The reconstruction procedure is cohesive in terms of similarity and picture quality, according to the same trend. The same trend indicates that the reconstruction process is coherent regarding similarity and image quality.

The Cumulative distribution function (CDF) of the error ratio R of the proposed EMGAN and other models is shown in Figure 10.As illustrated in Figure 10a, the proposed EMGAN model outperforms the kriging and EME-Net methods. In addition, Figure 10b shows that, despite the optimistic visual evaluation, the performance of the proposed

Preprints (www.preprints.org) | NOT PEER-REVIEWED | Posted: 2 November 2022 doi:10.20944/preprints202211.0040.v1

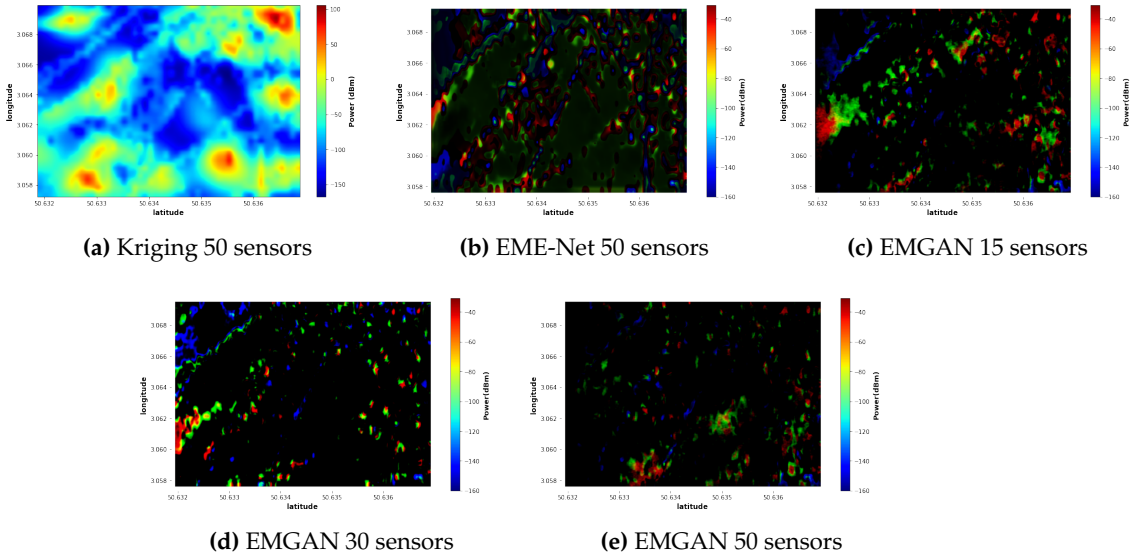

(a) Kriging 50 sensors **(b)** EME-Net 50 sensors **(c)** EMGAN 15 sensors

(d) EMGAN 30 sensors **(e)** EMGAN 50 sensors

Figure 8. Error maps of the proposed EMGAN for different number of sensors and EME-Net model.

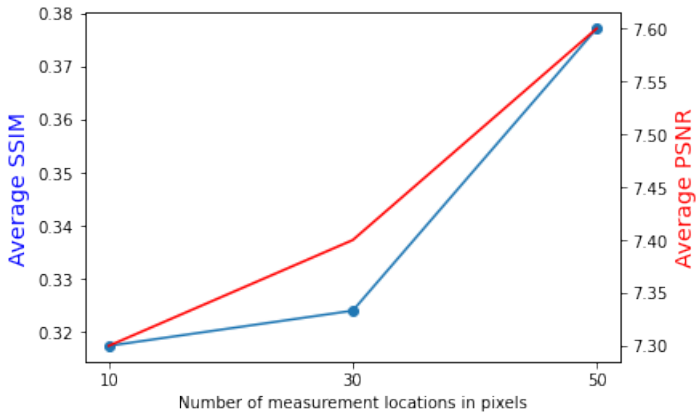

Figure 9. Average SSIM and PSNR of the proposed EMGAN with a varying number of measurement points.

EMGAN degrades as the number of sensors decreases. On the 1 km^2 area we are studying, the 50 sensors are needed to avoid some large deviations.

In Figure 11, the probability density function (PDF) of the ratio between the reconstructed maps and the ground truth of the proposed EMGAN model with different numbers of sensors, EME-Net, and simple kriging methods are presented. The error ratio (in dB) distribution can be well approximated by a Gaussian random variable. We first notice that the mean is rather close to 0, meaning there is no significant bias in the prediction steps. The second important point is that we note the reduction of the variance with the increase of the sensor of numbers. With 50 sensors in the studied 1 km^2 area, the variance is reduced to 0.85, which seems a reasonable value for an exposimetry study, resulting in more than 90% of the error ratio below 3dB. We also notice that the EME-Net approach with 50 sensors is not as good as the proposed approach with 30.

Preprints (www.preprints.org) | NOT PEER-REVIEWED | Posted: 2 November 2022 doi:10.20944/preprints202211.0040.v1

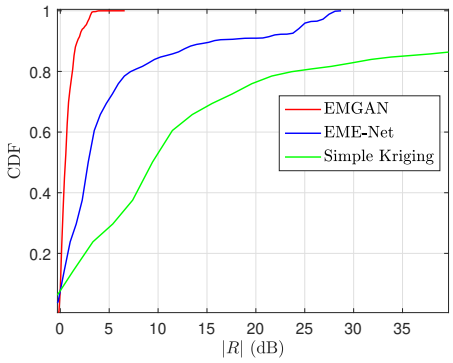

(a) Different models

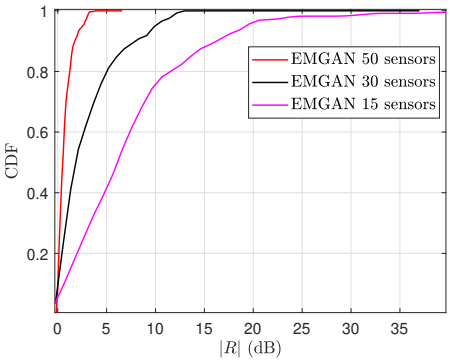

(b) EMGAN with varying number of sensors

Figure 10. CDF of the models as function of the absolute ratio $|R|$ between the reconstructed map and ground truth.

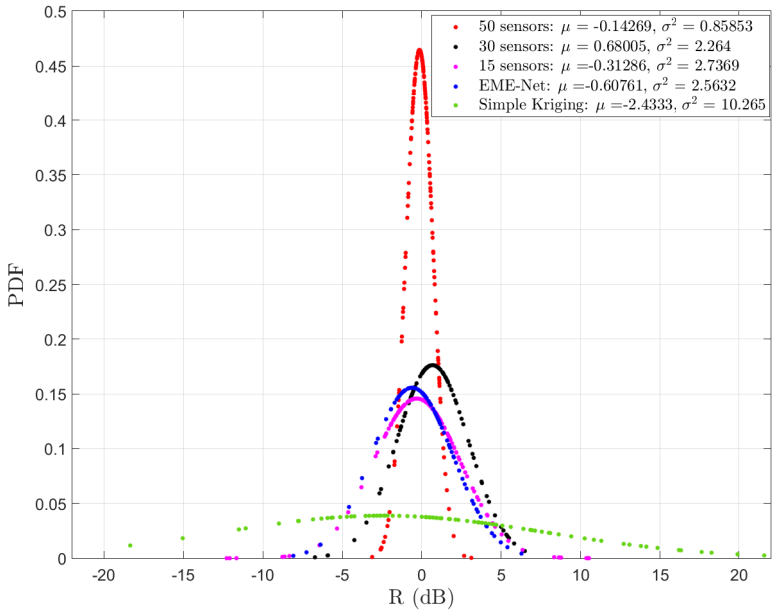

Figure 11. The probability density of the ratio R between the reconstructed map and ground truth when different numbers of sensors are used.

6. Conclusion

In this work, we present the EMGAN methodology, a deep learning-based exposure maps estimation method for urban environment. The generator and the discriminator are developed to estimate the exposure maps and improve the estimation accuracy by incorporating the city topology as a conditional input to the model. Instead of making direct, inaccurate, or biased assumptions about radio propagation, the EMGANs algorithm learns and uses radio environment information from the training process. The EMGANs algorithm offers a highly accurate estimation performance, significantly more accurate than traditional approaches, according to experimental data. Future work will concentrate on expanding the estimation of exposure maps using EMGANs to the temporal dimension.

7. Acknowledgement

The French government's Beyond5G initiative, which was sponsored as a component of the country's future investment program and strategy for economic recovery, provided

partial funding for this project. The location of this research is IRCICA, USR CNRS 3380, Lille. The Métropole Européenne de Lille (MEL) is especially acknowledged for its support of this PhD thesis. The COST action CA20120 INTERACT is another funding source for this project.

Author Contributions: M.M., B.A., A.T., E.E.L, J.G., R.K., D.G.,J.W., L.C. contributed equally to this work. All authors have read and agreed to the published version of the manuscript.

Funding: This research work is done at IRCICA, USR CNRS 3380,Lille. Special Thanks to Métropole Européenne de Lille (MEL) for supporting this PhD project

Conflicts of Interest: The authors declare no conflict of interest.

References

1. Niknejad, A.M.; Thyagarajan, S.; Alon, E.; Wang, Y.; Hull, C. A circuit designer's guide to 5G mm-wave. In Proceedings of the 2015 IEEE Custom Integrated Circuits Conference (CICC), 2015, pp. 1–8. https://doi.org/10.1109/CICC.2015.7338410.
2. Ahokangas, P.; Matinmikko-Blue, M.; Yrjölä, S.; Hämmäinen, H. Platform configurations for local and private 5G networks in complex industrial multi-stakeholder ecosystems. *Telecommunications Policy* **2021**, *45*, S0308596121000331.
3. Gajšek, P.; Ravazzani, P.; Wiart, J.; Grellier, J.; Samaras, T.; Thuróczy, G. Electromagnetic field exposure assessment in Europe radiofrequency fields (10 MHz–6 GHz). *Journal of exposure science & environmental epidemiology* **2015**, *25*, 37–44.
4. on Non-Ionizing Radiation Protection, I.C.; et al. Guidelines for limiting exposure to electromagnetic fields (100 KHz to 300 GHz). *Health physics* **2020**, *118*, 483–524.
5. Bailey, W.H.; Bodemann, R.; Bushberg, J.; Chou, C.K.; Cleveland, R.; Faraone, A.; Foster, K.R.; Gettman, K.E.; Graf, K.; Harrington, T.; et al. Synopsis of IEEE Std C95. 1™-2019 "IEEE Standard for Safety Levels With Respect to Human Exposure to Electric, Magnetic, and Electromagnetic Fields, 0 Hz to 300 GHz". *IEEE Access* **2019**, *7*, 171346–171356.
6. Mirza, M.; Osindero, S. Conditional generative adversarial nets. *arXiv preprint arXiv:1411.1784* **2014**.
7. MacCartney, G.R.; Zhang, J.; Nie, S.; Rappaport, T.S. Path loss models for 5G millimeter wave propagation channels in urban microcells. In Proceedings of the 2013 IEEE Global Communications Conference (GLOBECOM), 2013, pp. 3948–3953. https://doi.org/10.1109/GLOCOM.2013.6831690.
8. Piersanti, S.; Annoni, L.A.; Cassioli, D. Millimeter waves channel measurements and path loss models. In Proceedings of the 2012 IEEE International Conference on Communications (ICC), 2012, pp. 4552–4556. https://doi.org/10.1109/ICC.2012.6363950.
9. Andersen, J.; Rappaport, T.; Yoshida, S. Propagation measurements and models for wireless communications channels. *IEEE Communications Magazine* **1995**, *33*, 42–49. https://doi.org/10.1109/35.339880.
10. Wahl, R.; Wölfle, G.; Wertz, P.; Wildbolz, P.; Landstorfer, F. Dominant path prediction model for urban scenarios. *14th IST Mobile and Wireless Communications Summit, Dresden (Germany)* **2005**.
11. Rizk, K.; Wagen, J.F.; Gardiol, F. Two-dimensional ray-tracing modeling for propagation prediction in microcellular environments. *IEEE Transactions on Vehicular Technology* **1997**, *46*, 508–518.
12. Balanis, C.A. *Advanced engineering electromagnetics*; John Wiley & Sons, 2012.
13. Zugno, T.; Drago, M.; Giordani, M.; Polese, M.; Zorzi, M. Toward standardization of millimeter-wave vehicle-to-vehicle networks: Open challenges and performance evaluation. *IEEE Communications Magazine* **2020**, *58*, 79–85.
14. Yun, Z.; Iskander, M.F. Ray tracing for radio propagation modeling: Principles and applications. *IEEE access* **2015**, *3*, 1089–1100.
15. Boban, M.; Barros, J.; Tonguz, O.K. Geometry-based vehicle-to-vehicle channel modeling for large-scale simulation. *IEEE Transactions on Vehicular Technology* **2014**, *63*, 4146–4164.
16. Stein, M.L. *Interpolation of spatial data: some theory for kriging*; Springer Science & Business Media, 1999.
17. Knotters, M.; Brus, D.; Voshaar, J.O. A comparison of kriging, co-kriging and kriging combined with regression for spatial interpolation of horizon depth with censored observations. *Geoderma* **1995**, *67*, 227–246.

18. Tesfay, A.A.; Clavier, L. Gaussian Process-based Spatial Reconstruction of Electromagnetic fields, 2022. https://doi.org/10.48550/ARXIV.2203.01869.
19. Han, X.; Xue, L.; Shao, F.; Xu, Y. A Power Spectrum Maps Estimation Algorithm Based on Generative Adversarial Networks for Underlay Cognitive Radio Networks. *Sensors* **2020**, *20*. https://doi.org/10.3390/s20010311.
20. Goodfellow, I.; Pouget-Abadie, J.; Mirza, M.; Xu, B.; Warde-Farley, D.; Ozair, S.; Courville, A.; Bengio, Y. Generative adversarial nets. *Advances in neural information processing systems* **2014**, *27*.
21. Imai, T.; Kitao, K.; Inomata, M. Radio propagation prediction model using convolutional neural networks by deep learning. In Proceedings of the 2019 13th European Conference on Antennas and Propagation (EuCAP). IEEE, 2019, pp. 1–5.
22. Saito, K.; Jin, Y.; Kang, C.; Takada, J.i.; Leu, J.S. Two-step path loss prediction by artificial neural network for wireless service area planning. *IEICE Communications Express* **2019**.
23. LeCun, Y.; Bottou, L.; Bengio, Y.; Haffner, P. Gradient-based learning applied to document recognition. *Proceedings of the IEEE* **1998**, *86*, 2278–2324.
24. Popoola, S.I.; Jefia, A.; Atayero, A.A.; Kingsley, O.; Faruk, N.; Oseni, O.F.; Abolade, R.O. Determination of neural network parameters for path loss prediction in very high frequency wireless channel. *IEEE access* **2019**, *7*, 150462–150483.
25. Sotiroudis, S.P.; Goudos, S.K.; Gotsis, K.A.; Siakavara, K.; Sahalos, J.N. Application of a composite differential evolution algorithm in optimal neural network design for propagation path-loss prediction in mobile communication systems. *IEEE Antennas and Wireless Propagation Letters* **2013**, *12*, 364–367.
26. Popescu, I.; Nafomita, I.; Constantinou, P.; Kanatas, A.; Moraitis, N. Neural networks applications for the prediction of propagation path loss in urban environments. In Proceedings of the IEEE VTS 53rd Vehicular Technology Conference, Spring 2001. Proceedings (Cat. No. 01CH37202). IEEE, 2001, Vol. 1, pp. 387–391.
27. Teganya, Y.; Romero, D. Deep completion autoencoders for radio map estimation. *IEEE Transactions on Wireless Communications* **2021**.
28. Zhang, Y. A better autoencoder for image: Convolutional autoencoder. In Proceedings of the ICONIP17-DCEC. Available online: http://users. cecs. anu. edu. au/Tom. Gedeon/conf/ABCs2018/paper/ABCs2018_paper_58. pdf (accessed on 23 March 2017), 2018.
29. Egea-Lopez, E.; Losilla, F.; Pascual-Garcia, J.; Molina-Garcia-Pardo, J.M. Vehicular networks simulation with realistic physics. *IEEE Access* **2019**, *7*, 44021–44036.
30. Lopez, P.A.; Behrisch, M.; Bieker-Walz, L.; Erdmann, J.; Flötteröd, Y.P.; Hilbrich, R.; Lücken, L.; Rummel, J.; Wagner, P.; Wießner, E. Microscopic Traffic Simulation using SUMO. In Proceedings of the The 21st IEEE International Conference on Intelligent Transportation Systems. IEEE, 2018.
31. Egea-Lopez, E.; Molina-Garcia-Pardo, J.M.; Lienard, M.; Degauque, P. Opal: An open source ray-tracing propagation simulator for electromagnetic characterization. *Plos one* **2021**, *16*, e0260060.
32. OpenStreetMap contributors. Planet dump retrieved from https://planet.osm.org . https://www.openstreetmap.org, 2017.
33. Xu, C.; Zhao, B. Satellite image spoofing: Creating remote sensing dataset with generative adversarial networks (short paper). In Proceedings of the 10th International conference on geographic information science (GIScience 2018). Schloss Dagstuhl-Leibniz-Zentrum fuer Informatik, 2018.
34. Sun, J.; Du, Y.; Li, C.; Wu, T.H.; Yang, B.; Mok, G.S. Pix2Pix generative adversarial network for low dose myocardial perfusion SPECT denoising. *Quantitative Imaging in Medicine and Surgery* **2022**, *12*, 3539.
35. Isola, P.; Zhu, J.Y.; Zhou, T.; Efros, A.A. Image-to-image translation with conditional adversarial networks. In Proceedings of the Proceedings of the IEEE conference on computer vision and pattern recognition, 2017, pp. 1125–1134.
36. RGBA color model, 2021. Page Version ID: 1057086643.
37. Wang, Z.; Bovik, A.C.; Sheikh, H.R.; Simoncelli, E.P. Image quality assessment: from error visibility to structural similarity. *IEEE transactions on image processing* **2004**, *13*, 600–612.
38. Mallik, M.; Kharbech, S.; Mazloum, T.; Wang, S.; Wiart, J.; Gaillot, D.; Clavier, L. EME-Net: A U-net-based Indoor EMF Exposure Map Reconstruction Method. In Proceedings of the 2022 16th European Conference on Antennas and Propagation (EuCAP); , 2022.